NANO · MICRO small
www.small-journal.com

Biomimetic Transparent Nanoplasmonic Meshes by Reverse-Nanoimprinting for Bio-Interfaced Spatiotemporal Multimodal SERS Bioanalysis

*Aditya Garg, Elieser Mejia, Wonil Nam, Peter Vikesland, and Wei Zhou**

Multicellular systems, such as microbial biofilms and cancerous tumors, feature complex biological activities coordinated by cellular interactions mediated via different signaling and regulatory pathways, which are intrinsically heterogeneous, dynamic, and adaptive. However, due to their invasiveness or their inability to interface with native cellular networks, standard bioanalysis methods do not allow in situ spatiotemporal biochemical monitoring of multicellular systems to capture holistic spatiotemporal pictures of systems-level biology. Here, a high-throughput reverse nanoimprint lithography approach is reported to create biomimetic transparent nanoplasmonic microporous mesh (BTNMM) devices with ultrathin flexible microporous structures for spatiotemporal multimodal surface-enhanced Raman spectroscopy (SERS) measurements at the bio-interface. It is demonstrated that BTNMMs, supporting uniform and ultrasensitive SERS hotspots, can simultaneously enable spatiotemporal multimodal SERS measurements for targeted pH sensing and non-targeted molecular detection to resolve the diffusion dynamics for pH, adenine, and Rhodamine 6G molecules in agarose gel. Moreover, it is demonstrated that BTNMMs can act as multifunctional bio-interfaced SERS sensors to conduct in situ spatiotemporal pH mapping and molecular profiling of *Escherichia coli* biofilms. It is envisioned that the ultrasensitive multimodal SERS capability, transport permeability, and biomechanical compatibility of the BTNMMs can open exciting avenues for bio-interfaced multifunctional sensing applications both in vitro and in vivo.

1. Introduction

For multicellular systems, such as microbial biofilms and cancerous tumors, it is essential to capture the holistic system-level spatiotemporal picture to understand complex and dynamically evolving biological activities and to determine effective therapeutic intervention methods.[1,2]

For example, we know that microorganisms in biofilms can better resist antibiotic exposure or host immune response via multiple mechanisms,[3–5] including extracellular polymeric substances (EPS) diffusion barrier,[4] metabolic dormancy,[5,6] antibiotic resistance gene transfer,[7] quorum sensing,[8] and polymicrobial synergism.[9] Unfortunately, there are few methods for monitoring spatiotemporal biofilm activities that allow the investigation of how these different survival mechanisms interplay to affect system-level biofilm responses. Standard chemical bioanalysis methods in microbiology studies can be categorized as ex situ (off-site) or in situ (on-site). Among ex situ bioanalysis techniques, targeted molecular detection methods, including polymerase chain reaction (PCR) based tests and immunoassays, are the traditional tools used to identify genetic or proteomic markers for known microbes.[10] Non-targeted molecular profiling methods based on mass spectrometry (MS) or nuclear magnetic resonance (NMR) spectroscopy are powerful discovery-based ex situ metabolomics tools used to characterize the metabolic response of living systems to environmental, pathophysiological, or genetic perturbations.[11] Despite their strength in analytical quantification, standard ex situ bioanalysis methods are destructive and cannot resolve the spatiotemporal activities of multicellular systems to study genotypic/phenotypic variations between subpopulations. Standard in situ bioanalyses for biofilms rely on fluorescence microscopy imaging of probe-labeled cellular components,[12] which can measure spatial distributions of microbes in biofilms. Unfortunately, such label-based imaging approaches are invasive to living cells due to staining and cannot be used to map longitudinal biochemical activities (e.g., metabolic responses) in living biofilms. Recently, biosensing techniques, which exploit surface-functionalized receptors to

A. Garg, E. Mejia, W. Nam, W. Zhou
Department of Electrical and Computer Engineering
Virginia Tech
Blacksburg, VA 24061, USA
E-mail: wzh@vt.edu
P. Vikesland
Department of Civil and Environmental Engineering
Virginia Tech
Blacksburg, VA 24061, USA
The ORCID identification number(s) for the author(s) of this article can be found under https://doi.org/10.1002/smll.202204517.

DOI: 10.1002/smll.202204517

detect targeted biomarkers, have emerged for in situ biochemical monitoring of living systems.[13] However, existing biosensors cannot perform holistic non-targeted molecular profiling for discovery-based biological studies. Furthermore, typical biosensing systems based on rigid planar substrates are unsuitable for interfacing with 3D microbial biofilm networks in clinically relevant situations (e.g., wound or implant surfaces).

As a nano-enabled ultrasensitive vibrational biosensing-bioanalysis technique, surface-enhanced Raman spectroscopy (SERS) enjoys the advantages of noninvasive measurements, minimal sample preparation, and no water background interference.[14] Uniquely, SERS can operate either in targeted or non-targeted modalities. Targeted SERS uses surface-functionalized reporter molecules to detect specific analytes (e.g., proteins, nucleic acids)[15] or physical properties of the local environment (e.g., pH, temperature).[16] Although targeted SERS assays in the sandwich immunoassay format are not suitable for the spatiotemporal analysis of living biosystems due to the need for a secondary capture probe, targeted SERS assays where the vibrational frequency of SERS labels change in response to the target molecules[17] or changes in environmental parameters[18] can be employed. Non-targeted SERS measures the fingerprint profiles of molecule ensembles in SERS hotspots and requires multivariate analysis via methods such as machine learning approaches.[19,20] For the in situ biochemical analysis of living multicellular systems, it is highly desirable to perform multimodal spatiotemporal SERS measurements in both non-targeted and targeted modalities as they can provide complementary information. For example, bacterial biofilm development processes are spatiotemporally coupled with changes in local pH and biomolecule (e.g., intercellular signaling molecules, nutrients, and waste products) concentrations. These processes generate a heterogeneous distribution of bacterial subpopulations within the biofilms. Since specific subpopulations in the microbial community serve defined roles such as dormant cells that can withstand antibiotic attacks, resolving the spatiotemporal evolution of pH and different biochemical components can potentially assist therapeutic intervention.[2,21–23] However, implementing multimodal spatiotemporal SERS bioanalysis in both targeted and non-targeted modalities remains a formidable challenge primarily because surface-functionalized SERS substrates provide weak label-free signals from target molecules due to the spatial competition of occupation between the Raman reporter molecules and the non-targeted analyte molecules at the SERS hotspots.

Defined by their spatial hotspot arrangement, SERS devices are characterized as unbound or surface-bound.[24] Unbound SERS devices based upon discrete plasmonic nanoparticles can intimately interface with cells, but suffer from poor spatiotemporal reproducibility because of the uncontrolled diffusion, aggregation, and distribution of the randomly organized nanoparticles. Surface-bound SERS devices,[25] often created by top-down nanofabrication, carry mechanically stabilized plasmonic hotspots in uniform arrays for reliable spatiotemporal measurements. To date, surface-bound SERS devices typically exhibit a continuous planar form since conventional nanofabrication processes, such as electron beam lithography (EBL)[26] and deep-ultraviolet lithography (DUVL),[27] rely on planar spin-coating and flat substrate lithography. However, continuous planar SERS devices elicit a poor nano-bio interface with native cellular networks due to the mismatch in their mechanical, topological, and permeable properties. To overcome such difficulties, we have recently developed microporous nanolaminated plasmonic crystal meshes that can interface dense and uniform hotspot arrays with biosystems for in situ spatiotemporal SERS bioanalysis.[28] However, microporous nanolaminated plasmonic crystal meshes are opaque and thus cannot allow multi-stacked operation for spatiotemporal multimodal SERS measurements of multicellular systems in both non-targeted and targeted detection modalities (Text S1 and Figures S1 and S2, Supporting Information).

This work reports a novel high-throughput reverse nanoimprint lithography (RNIL) approach to create biomimetic transparent nanoplasmonic microporous mesh (BTNMM) devices for spatiotemporal multimodal SERS measurements at the bio-interface. We demonstrate that the BTNMMs, carrying dense nanolaminated plasmonic nanoantenna (NLPNA) arrays that support multiple hybrid localized surface plasmon modes with spatial mode overlap,[29] can serve as highly sensitive SERS devices for spatiotemporal multimodal SERS measurements for targeted pH sensing and non-targeted molecular detection to resolve the diffusion dynamics for pH, adenine, and Rhodamine 6G (R6G) molecules in agarose gel. As a proof-of-concept application, we demonstrate that the BTNMMs can perform multifunctional bio-interfaced sensing to conduct in situ spatiotemporal multimodal SERS analysis of *Escherichia coli* (*E. coli*) biofilms for targeted pH sensing and non-targeted molecular detection.

2. Fabrication of BTNMMs

The fabrication processes implemented to generate the BTNMMs are depicted in **Figure 1**A. First, polymethyl methacrylate (PMMA) solution in anisole was spin-coated onto hydrophobic perfluoropolyether (PFPE) nanopillar array molds. Anisole, exhibiting a low surface tension, can wet the hydrophobic PFPE mold allowing conformal coating of the PMMA solution on the nanostructured PFPE surface. The thickness of the PMMA layer was optimized by controlling the spin-coating parameters (Figure S4, Supporting Information). This ensured that the PMMA layer thickness did not exceed the nanopillar height to generate PMMA nanohole arrays (NHAs) within the PFPE molds. Then, thermal RNIL was exploited to transfer the PMMA NHAs onto SU-8 microwell arrays patterned on silicon wafers with a sacrificial layer coating. The low surface energy of PFPE facilitates the RNIL process by allowing easy detachment of the PFPE mold from the imprinted PMMA NHAs. At the same time, the high elastic modulus of PFPE with good mechanical stability at high temperatures prevents buckling of the PFPE nanopillars at high temperatures during the RNIL process.[30] As shown in Figure 1B, uniformly structured NHAs were transferred onto the SU-8 microwell arrays over large areas with an excellent transfer yield. Mild reactive ion etching (RIE) was performed in oxygen plasma to remove the residual PMMA layer and tune the diameter of the PMMA nanoholes (Figure S5, Supporting Information). Then, we deposited alternating Au (25 nm) and SiO_2 (8 and 12 nm from bottom to top)

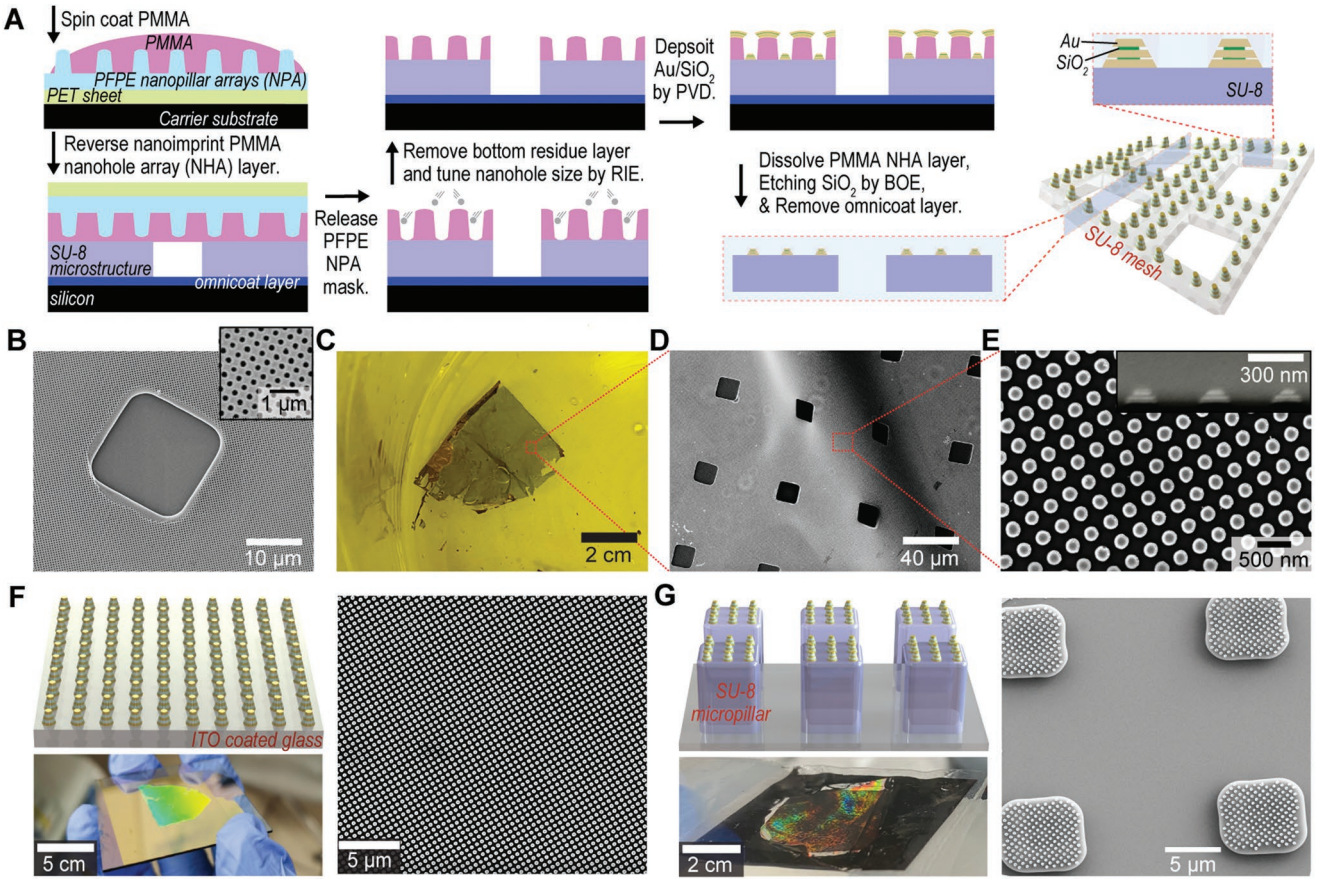

Figure 1. Fabrication of BTNMMs. A) Schematic illustration of the fabrication processes. B) SEM images of the PMMA nanohole arrays patterned on SU8 microwell arrays. C) Optical image of a freestanding BTNMM floating in an aqueous solution. D) Top-down SEM image of the BTNMM. E) Zoomed-in top-down SEM image and cross-sectional view SEM image of NLPNAs on the BTNMM. Schematic illustration, optical image, and top-down SEM image of NLPNAs integrated onto F) a planar ITO glass substrate and G) SU8 micropillar arrays.

layers within the PMMA NHAs by electron beam evaporation. We selected the metal and dielectric thicknesses to achieve multiresonant plasmonic responses across a broad range in the visible to near-infrared region.[29,31] Then, PMMA was dissolved to generate the NLPNAs, partial etching of the SiO_2 layers was performed to open the plasmonic nanogap hotspots,[32] and the sacrificial layer was eliminated to obtain freestanding BTNMM. Figure 1C depicts an optical image of the BTNMM in an aqueous solution, illustrating the ultra-flexibility of the BTNMM and the broadband absorption in visible frequencies indicated by the dark appearance of the BTNMM. The top-down view scanning electron microscope (SEM) images depict the microporous structure (periodicity = 64 μm, pore size = 16 μm) of the BTNMM and the uniformly shaped periodic plasmonic nanostructures on the polymeric scaffold, while the cross-sectional SEM image depicts the multilayered out-of-plane Au and SiO_2 nanodisks of the NLPNAs (Figure 1D,E). Compared to the conventional method to generate arrays of nanoparticles using freestanding Au NHAs as a physical deposition mask,[33] our method offers several unique advantages: 1) significantly higher throughput and reduced cost of generating NHA physical deposition masks using polymeric molding with reusable PFPE nanopillar molds, 2) facile transfer of the polymeric NHA mask onto the micro/nanostructured substrates via RNIL, 3) generation of uniformly shaped multilayered nanodisks over large areas via line-of-sight deposition due to the continuous and conformal contact between the polymeric NHA mask and the micro/nanostructured substrate (Figure 1B,E), and 4) easy tunability of the diameter of the nanoholes via RIE. Since a conformal and continuous contact is generated between the polymeric nanohole array and carrier substrates via RNIL, our fabrication method can potentially enable the facile transfer of NLPNAs, exhibiting a nanoscale footprint, onto various micro/nanostructured electrical or optical devices for multifunctional operation at the nanoscale.[34] To illustrate the versatility of the fabrication technique, NLPNAs were integrated with conductive indium tin oxide (ITO) coated glass slides (Figure 1F), and SU8 micropillar structures (Figure 1G).

3. Plasmonic Mode Engineering for Optimized SERS Performance

To optimize the SERS performance of the BTNMM, we first engineered the resonant wavelength positions of the plasmonic modes by tailoring the base diameter of the NLPNAs. The transferred nanohole diameter closely matches the original master mold, which is nominally 150 nm (**Figure 2**A; Figure S3,

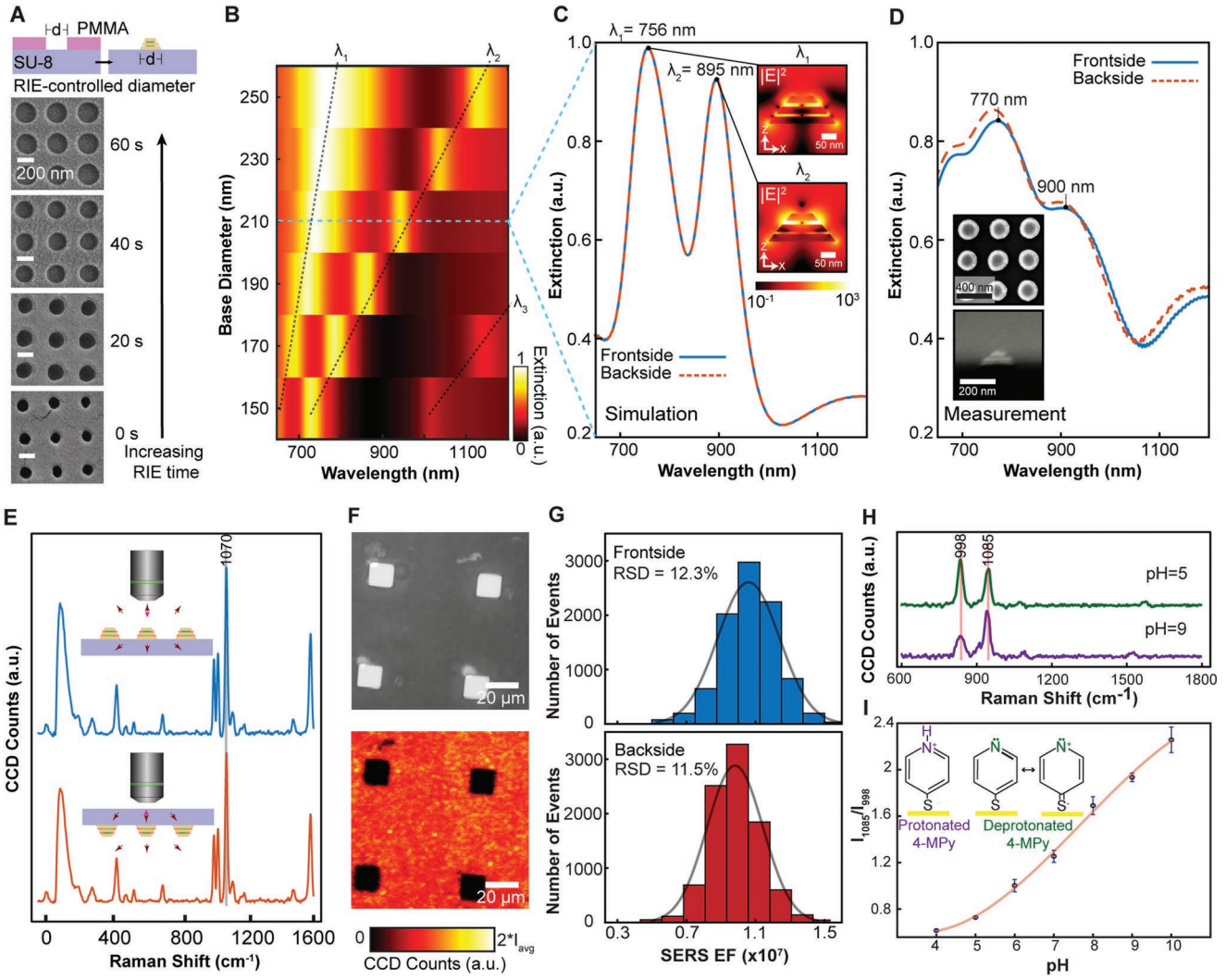

Figure 2. Optical properties and SERS performance of BTNMMs. A) SEM images of PMMA nanohole arrays after RIE treatment for 0, 20, 40, and 60 s. All scale bars in SEM images are 200 nm. B) FDTD-calculated extinction map of NLPNAs with different base nanodisk diameters ranging from 150 to 250 nm. C) FDTD-calculated extinction spectra of NLPNAs with a base nanodisk diameter of 210 nm under the front and backside light illumination. Inset shows FDTD-calculated $|E|^2$ distribution maps in the *x-z* plane for two modes at 756 and 895 nm. D) Measured extinction spectra of NLPNAs on BTNMMs under the front and backside illumination. Inset shows top-down and cross-section SEM images of the NLPNAs. E) Measured average SERS spectra of BZT molecules from NLPNAs on BTNMMs under 785 nm laser excitation from the front and back sides. F) Bright-field microscopy image of a BTNMM and the corresponding 2D Raman image for the BZT Raman peak at 1077 cm^{-1}. G) Histograms of the SERS EFs measured at 1077 cm^{-1} from NLPNAs on the BTNMM under frontside and backside laser excitation. H) The measured 4-MPy SERS spectra from NLPNAs on the BTNMMs soaked in PBS solution with pH values of 5 and 9. I) The dependence of I_{1085}/I_{998} on the pH values between 4 and 10 in PBS solution. The red line represents the best-fit curve for the plot.

Supporting Information). Mild RIE enabled us to expand the initial nanohole diameter from ≈150 to ≈250 nm by increasing the RIE time from 0 to 60 s (Figure 2A). Hence, RIE can provide a way to tailor the base diameter of the NLPNAs to fine-tune the resonant wavelength positions of the plasmonic modes without relying on multiple mold templates with different diameters. Based on the possible range of base diameters, we obtained the calculated 2D extinction map from finite-difference time-domain (FDTD) simulations in the wavelength range of 650–1200 nm (Figure 2B). With increasing NLPNA base diameter (D), the extinction map revealed a collective redshifting for three modes highlighted by a black dashed line in Figure 2B as λ_1, λ_2, and λ_3, respectively. The highest energy mode with the resonant peak at λ_1 redshifts from 657 to 767 nm, and the linewidth continuously broadens with increasing base diameter from 150 to 250 nm. The continuous redshifting and linewidth broadening effects with increasing diameter can be attributed to geometric depolarization effects associated with localized surface plasmon oscillation periods approaching the retardation time needed to polarize the gold nanodisks.[35] The mode peak at λ_2 has a relatively constant linewidth and redshifts from 730 to 1131 nm with increasing diameter. A low-energy mode is apparent in the extinction map for diameters between 150 and 170 nm with a redshifting trend from 1017 to 1140 nm, suggesting the mode

redshifts beyond 1200 nm for diameters greater than 190 nm. Based on the 2D extinction maps, we selected the diameter of 210 nm as λ_2 shows good spectral mode overlap with the excitation wavelength of 785 nm for SERS. Figure 2C shows the simulated extinction spectra for a diameter of 210 nm under frontside and backside illumination and the electric field intensity ($|E|^2$) distribution map for the resonant peaks. The two resonant peaks at $\lambda_1 = 756$ nm and $\lambda_2 = 895$ nm demonstrate a large electric field intensity enhancement ($|E|^2 > 10^3$). The λ_1 mode shows electric dipole characteristics with enhanced $|E|^2$ at the bottom metal-substrate interface and within top and bottom dielectric nanogap cavities. In contrast, λ_2 and λ_3 modes feature magnetic response, showing characteristics for antibonding magnetic dipole mode and bonding magnetic quadrupole mode, respectively.[31,36] Based on the FDTD simulation, we proceeded with the nanofabrication of NLPNAs with a target diameter of 210 nm, corresponding to an RIE etching time of 40 s. The measured extinction spectra in Figure 2D agree with simulations, demonstrating broad resonances at 770 and 900 nm.

After engineering the plasmonic modes for optimal SERS performance, we evaluated the SERS performance of the BTNMM under 785 nm laser excitation by generating a self-assembled monolayer of benzenethiol (BZT) molecules. The BZT molecules can act as a non-resonant Raman probe on the NLPNAs. The SERS spectra of BZT measured under illumination from the frontside and backside exhibit similar SERS signal intensities (Figure 2E). Figure 2F illustrates 2D Raman mapping of the BZT Raman peak at 1070 cm^{-1} over a 110 μm × 110 μm area containing 12 100 pixels, and the correlated bright-field image. The 2D Raman map shows uniform signal intensities demonstrating the large-area structural uniformity of the plasmonic hotspot array on the BTNMM. The corresponding histograms of the SERS enhancement factors (Efs) obtained using the 1070 cm^{-1} BZT Raman peak display a high SERS EF ($\approx 10^7$) and a normal distribution profile under frontside and backside excitation with a relative standard deviation (RSD) of 12.3% and 11.5%, respectively. These results statistically validate the uniform distribution of the ultrasensitive SERS hotspots on the polymeric scaffold (Figure 2G). For SERS pH measurements, 4-Mercaptopyridine (4-Mpy), which can form a self-assembled monolayer on gold surfaces via its thiol group, was used as the pH-sensitive Raman probe. The protonation/deprotonation of the heterocyclic nitrogen in 4-Mpy as a function of pH can be detected by SERS.[37,38] The SERS spectra of 4-Mpy in PBS at different pH values indicate that the intensity ratio between the ring breathing vibration mode at 998 cm^{-1} and the C–S band at 1085 cm^{-1} gradually decreased as the pH value of PBS increased (Figure 2H).[37] The peak ratio (I_{1085}/I_{998}) was plotted as a function of bulk pH to generate a working curve for SERS-enabled pH detection (Figure 2I).

4. Spatiotemporal Multimodal SERS Measurements in Targeted pH Sensing and Non-Targeted Molecular Detection

Multimodal spatiotemporal SERS measurements for targeted pH sensing and non-targeted molecular profiling can be achieved by stacking labeled and label-free BTNMMs. This outcome is due to several enabling features of the BTNMM: 1) the transport permeability of microporous meshes allows accessibility of analyte molecules to plasmonic hotspots on both SERS probes, 2) the ultrathin polymeric mesh structure ensures that the plasmonic hotspots of both SERS probes remain within the depth of focus of the objective lens, 3) the optical transparency enables laser excitation and backscattered Raman signal collection from the bottom SERS probe in the stacked configuration, and 4) the large-area structural uniformity of the NLPNA hotspot arrays enables reliable spatiotemporal SERS measurements. We assessed the potential of the BTNMMs for multimodal spatiotemporal monitoring of the diffusion dynamics of hydroxyl ions (i.e., resulting in changes in measured pH) and different analyte molecules, including adenine and R6G. In these experiments, we stack and embed 4-Mpy labeled and label-free BTNMMs in agarose gel and then add an alkaline solution containing 10^{-3} M R6G and 10^{-3} M adenine into a reservoir inside the agarose gel (**Figure 3**A,B). This localized solution delivery generates different diffusion concentration patterns for ions and analyte molecules, which can be resolved by time-dependent SERS mapping. The reservoir was refilled with the solution every six hours, and SERS mapping was performed at t = 0, 6, 12, 18, 24, and 30 h over a large area (4 × 4 mm^2). Figure 3C shows the average SERS spectra between 0 and 30 h. The signal intensities for Raman peaks were calibrated with the electronic Raman scattering (ERS) internal standard across different measurements.[39] At t = 0 h, the average SERS spectrum demonstrates peaks at 998 and 1085 cm^{-1} from 4-Mpy. At t = 6 h, a peak at 732 cm^{-1} originating from adenine appears, while at t = 18 h, several new peaks at 610, 773, 1185, 1310, 1360, and 1507 cm^{-1} emerge. These latter peaks originate from R6G.[40] The later emergence of the R6G peak can be attributed to the larger size of the R6G molecules compared to adenine molecules, leading to a slower diffusion rate of R6G.[41] To quantitatively analyze these temporal changes, we plotted the calibrated pH values and the ERS-calibrated Raman intensities of the adenine (732 cm^{-1}) and R6G (1360 cm^{-1}) peaks as a function of time (Figure 3E). First, we observe that the pH continuously increases with time from a mean value of ≈7 to ≈8.5 due to the constant influx of hydroxyl ions from the alkaline solution in the reservoir. Second, the adenine peak Intensity continually increases between 0 and 18 h and then is marginally reduced between 18 and 30 h. Concurrently, the R6G peak intensity continually increases between 12 and 30 h. The slight reduction in the Raman intensity of the adenine peak between 18 and 30 h can be attributed to the decreased spatial occupation of the SERS hotspots by the adenine molecules due to the increased adsorption of R6G molecules in the same hotspots.[40] To validate our observations, we developed a numerical model that quantitatively accounts for the spatiotemporal dynamics of the movement of hydroxyl ions, adenine molecules, and R6G molecules from the reservoir to the BTNMMs through the agarose gel (Text S2 and Figure S6, Supporting Information). Using our model, we plot the theoretical concentrations of hydroxyl ions, adenine molecules, and R6G molecules throughout the agarose gel at different time points (Figure S6B–D). Subsequently, we plot the theoretical concentrations of hydroxyl ions, adenine molecules, and R6G molecules

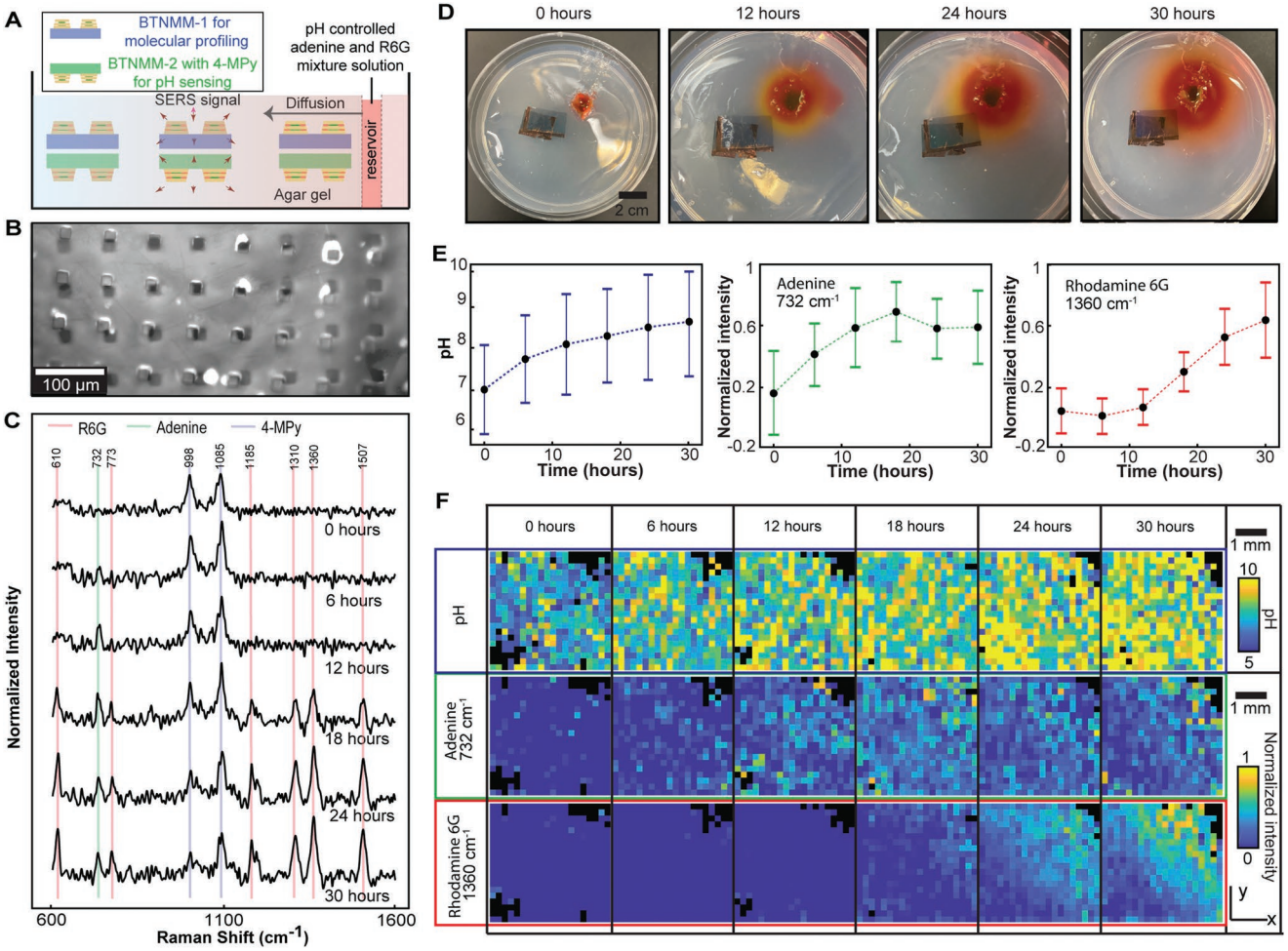

Figure 3. Spatiotemporal multimodal SERS measurements of the diffusion dynamics of hydroxyl ions, adenine molecules, and R6G molecules in agarose gel using stacked labeled and label-free BTNMMs. A) Schematic illustration of the experimental setup. B) Top-down bright field image of the stacked BTNMMs embedded in agarose gel. C) Average SERS spectra measured between 0 and 30 h. Note: green lines mark adenine peaks, red lines mark R6G peaks, and purple lines mark 4-MPy peaks. D) Top-down optical images at 0, 12, 24, and 30 h. E) The ERS-calibrated Raman intensities at 732 (adenine) and 1360 cm^{-1} (R6G), and the pH values measured between 0 and 30 h. F) 2D maps of the ERS-calibrated Raman intensities at 732 and 1360 cm^{-1}, and the correlated pH maps measured between 0 and 30 h. Black pixels represent eliminated spectra.

at the center of the analyzed region as a function of time (Figure S6E–G). Indeed, the modeled concentrations of hydroxyl ions, adenine molecules, and R6G molecules as a function of time at the analyzed region (Figure S6E–G) qualitatively match with the experimental SERS data (Figure 3E). These results validate that the differences in the diffusion dynamics of hydroxyl ions, adenine molecules, and R6G molecules in agarose gel are primarily responsible for the different temporal trends observed in the SERS data. To further analyze the spatial dynamics of the diffusion process, we plot the 2D maps of the calibrated pH values and the ERS-calibrated Raman intensities of the adenine (732 cm^{-1}) and R6G (1360 cm^{-1}) Raman peaks as a function of time (Figure 3F). First, the pH maps show no visible diffusion gradients since the small hydroxyl ions would diffuse rapidly across the agarose gel to establish a near-equilibrium state within 6 h (Figure S4B, Supporting Information). Notably, the non-uniform distribution of pH values in the 2D maps can be attributed to the non-uniform movement of ions in the gel due to interference from the nanoporous agarose network and deviations of some data points from the pH calibration curve due to random variations In the spatial orientation of 4-mPy at the SERS hotspots.[42] Second, the 2D maps of the adenine Raman peak reveal non-uniform concentration gradients across the sensor surface between 6 and 30 h due to the high diffusion rate of the small adenine molecules. In comparison, the spatiotemporal maps of the R6G Raman peak demonstrate uniform and temporally evolving concentration gradients between 18 and 30 h, depicting the slower diffusion dynamics of the larger R6G molecules. These results indicate that the BTNMMs can enable multimodal spatiotemporal SERS measurements by stacking the labeled and label-free mesh SERS sensors.

5. Bio-Interfaced Spatiotemporal pH mapping and Molecular Profiling of *E. coli* Biofilms

The BTNMMs offer significant biocompatibility advantages enabled by their mesh-like geometry and, therefore, can act as

bio-interfaced SERS devices for the simultaneous in situ analysis of the spatial and temporal dynamics of pH and molecular fingerprint signatures in biosystems. To illustrate the capability of the BTNMMs for bio-interfaced spatiotemporal multimodal monitoring of biosystems, we utilized our stacked mesh system to continuously monitor the pH and label-free biochemical signatures of growing *E. coli* bacterial biofilms for 48 h via SERS (**Figure 4**A). *E. coli* was seeded on the stacked BTNMMs interfaced with LB-agar plates, and bacterial colony proliferation was observed over time due to the nutrient supply into the biosystem from the LB-agar plates through the micropores of the BTNMMs (Figure 4B; Figure S7, Supporting Information). Figure 4C demonstrates the ERS-calibrated average SERS spectra between 2 and 48 h, and the assignments for the observed Raman peaks are provided in Table S1 (Supporting Information). We conducted spatiotemporal SERS measurements for 20×20 pixels over a 4×4 mm^2 region. At t = 2 h after seeding the *E. coli* cells, the SERS spectrum shows peaks at 998 and 1085 cm^{-1} from 4-mPy, a strong peak at 732 cm^{-1} from LB broth components, and peaks at 661 and 685 cm^{-1} from metabolites of purine degradation near the *E. coli* cells.[43] Compared to the stacked mesh system, a single 4-mPy labeled mesh did not exhibit peaks at 661, 685, and 732 cm^{-1} due to spatial occupation by the 4-mPy molecules within the SERS hotspots (Figure S8, Supporting

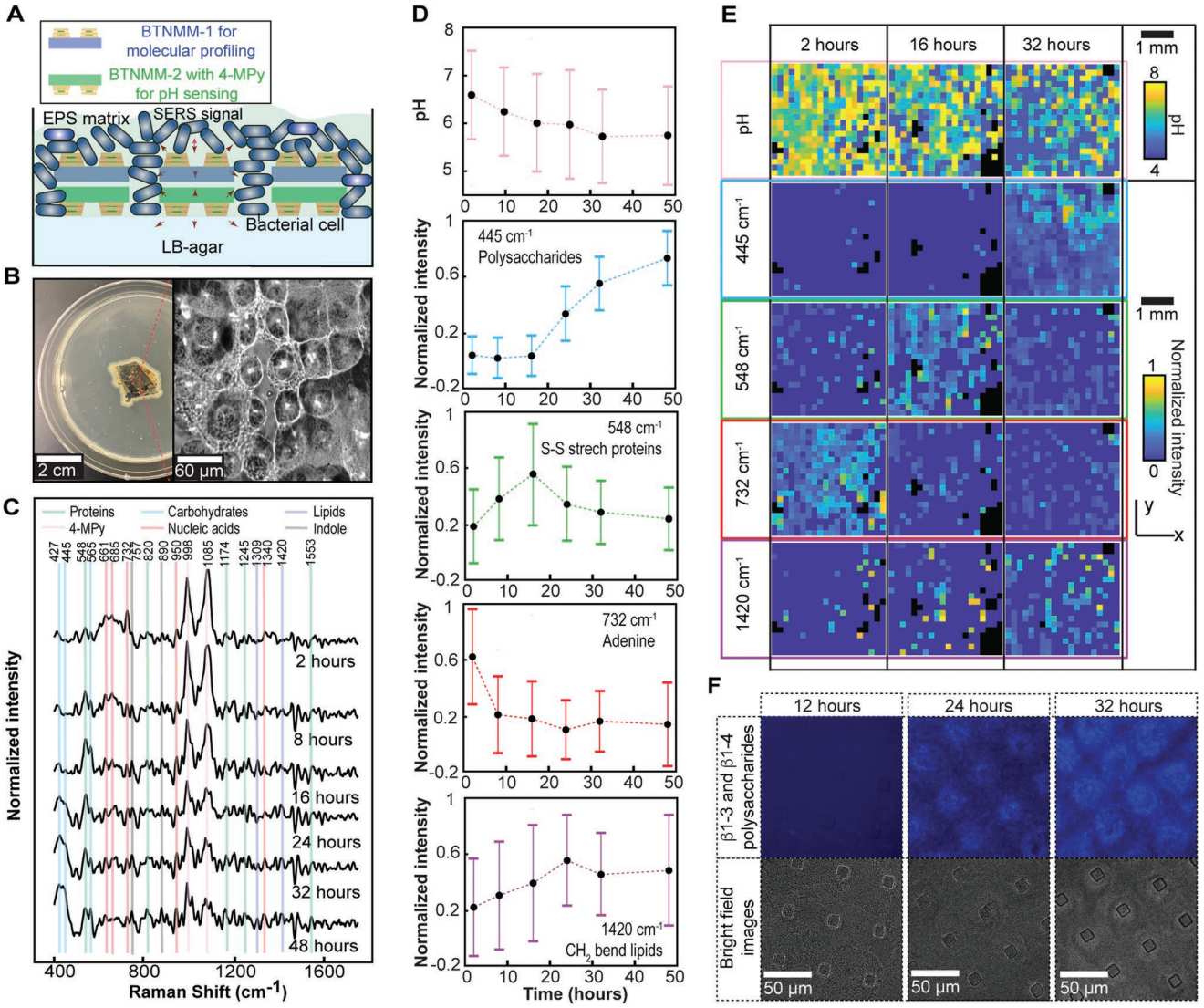

Figure 4. In situ spatiotemporal multimodal SERS measurements of *E. coli* biofilm development process with stacked BTNMMs in targeted pH sensing and non-targeted molecular detection. A) Schematic illustration of the experimental setup. B) Top-down camera and bright-field microscopy images of *E. coli* biofilms grown with BTNMMs on the LB agar plate at 24 h. C) Measured average SERS spectra of *E. coli* biofilms grown with BTNMMs between 2 and 48 h. Note: green lines mark protein peaks, red lines mark nucleic acid peaks, blue lines mark carbohydrate peaks, purple lines mark lipid peaks, grey lines mark indole peaks, and pink lines mark 4-MPy peaks. D) Time-dependent pH values and the ERS-calibrated Raman intensities at 445, 732, 548, and 1420 cm^{-1} by in situ multimodal SERS measurements of *E. coli* biofilms with BTNMMs at growth times from 2 to 48 h. E) Time-resolved 2D maps of the pH values and the ERS-calibrated Raman intensities at 445, 732, 548, and 1420 cm^{-1} by in situ spatiotemporal multimodal SERS measurements of *E. coli* biofilms with BTNMMs at growth times from 2 to 48 h. Black pixels represent eliminated spectra. F) Bright-field and fluorescence microscopy images of Calcofluor White (CW) stained biofilms at growth times of 12, 24, and 32 h.

Information). As the *E. coli* cell density increases from 0 to 16 h (Figure S5, Supporting Information), peaks attributed to components of the outer membrane of the *E. coli* cell wall, including proteins (548 cm^{-1}) and phospholipids (1309 cm^{-1}), emerge, indicating an intimate interface between the *E. coli* cells and the SERS hotspots.[44] In addition, peaks at 757 and 890 cm^{-1} attributed to indole, an extracellular signaling molecule secreted by *E. coli*, emerge.[45] With biofilm development from 16 to 48 h, we start to see several Raman peaks that are associated with biofilm EPS carbohydrates (427 and 445 cm^{-1}), proteins (820 and 1553 cm^{-1}), and lipids (1420 cm^{-1}).[46] Overall, the averaged label-free Raman spectra of *E. coli* biofilms at various growth stages from 400 pixels consist of highly overlapped and complex spectroscopic features that arise from the various biomolecules in the SERS hotspots within the area illuminated by the Raman laser across the measured region (Text S3 and Figure S9, Supporting Information). To quantitatively analyze the temporal pH and biomolecular changes during the growth of *E. coli* biofilms, we plot the calibrated pH values and ERS-calibrated Raman intensities of major peaks from carbohydrates, proteins, nucleic acids, and lipids as a function of time (Figure 4D). First, we observe that the pH continuously decreases as the biofilm develops from 2 to 48 h from a mean pH value of 6.8 to 5.5. This acidification of the microenvironment during biofilm development has been attributed to the by-products of bacterial carbohydrate metabolism such as acetic acid and lactic acid.[22,47] However, due to their low Raman cross-sections, these acids would be undetectable via SERS. Second, the peak intensity at 732 cm^{-1} (adenine) continually decreases between 2 and 48 h, reflecting the consumption of LB broth components by *E. coli*.[28] Third, we observe that peaks originating from cell wall components, including proteins (548 cm^{-1}) and phospholipids (1309 cm^{-1}), increase in intensity from 2 to 16 h as the *E. coli* cell density increases (Figure 4D; Figure S10, Supporting Information). Subsequently, these peaks from cell wall components decrease in intensity between 16 and 48 h. Concurrently, the peaks attributed to the EPS carbohydrates (427 and 445 cm^{-1}), proteins (820 cm^{-1}), and lipids (1420 cm^{-1}) rapidly increase after 16 h (Figure 4D; Figure S10, Supporting Information). These observations indicate that the SERS hotspots encounter reduced access to cell membrane components and increased access to EPS components as the *E. coli* biofilm develops.[48] The large standard deviations observed in Figure 4D reflect the non-uniform distribution of chemical species and heterogeneous pH microenvironments in the biological matrix (Text S2, Supporting Information). Figure 4E shows the 2D Raman maps of the pH values and major Raman bands during biofilm development at 2, 16, and 32 h. The spatiotemporal maps demonstrate a non-unform and dynamically changing spatial distribution of the different biomarkers, reflecting the heterogeneous structure and the complex spatiotemporal evolution of the biofilms on the mesh sensors.[21] For example, previous works have demonstrated the formation of spatially heterogeneous pH microenvironments in biofilms that are confined into discrete pockets of low pH due to the heterogeneous, three-dimensional, and porous architecture of biofilms.[22] To further understand the dynamic spatiotemporal evolution of the *E. coli* biofilms on the mesh sensors, we performed fluorescence imaging using Calcofluor White (CW) dyes. CW selectively binds to β-linked polysaccharides, which are major components of the EPS matrix of *E. coli* ATCC 25922 biofilms.[49] The fluorescence images (Figure 4F) indicate that the biovolume of β-linked polysaccharides continually increases between 12, 24, and 32 h, agreeing with our SERS results. As time increases from 12 to 24 h, the CW fluorescence signals emerge from the edges of the mesh pores indicating that the EPS matrix generation first occurs near the mesh pores due to the availability of nutrients from the LB-infused agar substrates.[50] As time increases to 32 h, CW fluorescence signals spread into regions beyond the mesh pores, manifesting an outward expansion of the growing biofilm from mesh pores (Figure 4F; Figure S11, Supporting Information).

6. Multivariate SERS Analysis and Classification of *E. coli* Biofilm Development Phases

For analyzing the inhomogeneous multivariable SERS dataset containing information regarding the molecular profile and the pH distribution of the growing biofilms, we employed multivariate chemometric techniques. We hierarchically implemented principal component analysis (PCA) and linear discriminant analysis (LDA) for analyzing and classifying the dataset from various biofilm development stages. For the analysis, we input the ERS calibrated label-free data from two spectral windows (400–950 and 1150–1600 cm^{-1}) and the labeled pH data for four different biofilm growth stages (2, 16, 32, and 48 h). The loading spectra of the first two principal components (PC1 and PC2) indicate that various spectral features strongly contribute to the loadings (**Figure 5**A). The PC1 loading spectrum illustrates that the peaks attributed to the EPS components such as polysaccharides (427 and 445 cm^{-1}), proteins (1174 and 1245 cm^{-1}), and lipids (1420 cm^{-1}) along with the pH data positively contribute to the loadings, while the peaks assigned to purines (661, 685, and 732 cm^{-1}) negatively contribute to the PC1 loadings. In addition, the peaks associated with the cell membrane components such as proteins (550 cm^{-1}) negatively contribute to the PC2 loading, while the peaks from purines (661, 685, and 732 cm^{-1}) positively contribute to the PC2 loading. Although we were able to assign the origins of various spectral components identified by the PC loadings using prior knowledge (Table S1, Supporting Information), further analysis would be required via conventional metabolomic techniques for the assignment of the unknown spectral features. In Figure 5B, the PC scatter plot shows two groups of overlapped scatters for the *E. coli* biofilms at a) 2 and 16 h and b) 32 and 48 h. Despite the significant contributions to the PC1 and PC2 loading plots from the spectral components related to the biofilms' molecular composition and pH distribution, the two PCs are insufficient to differentiate between the various stages of biofilm growth. Instead, PCA can serve as a data reduction tool to extract the significant variables, and subsequently, LDA can serve as the supervised learning method to classify the biofilm development stages using the first 150 PCs as the input variables. As shown in Figure 5C, the PCA-LDA classification model segregates the different *E. coli* biofilm growth stages. To assess the prediction ability of PCA-LDA model, we implemented the leave-one-out-cross-validation (LOOCV) method. The classification results demonstrate that

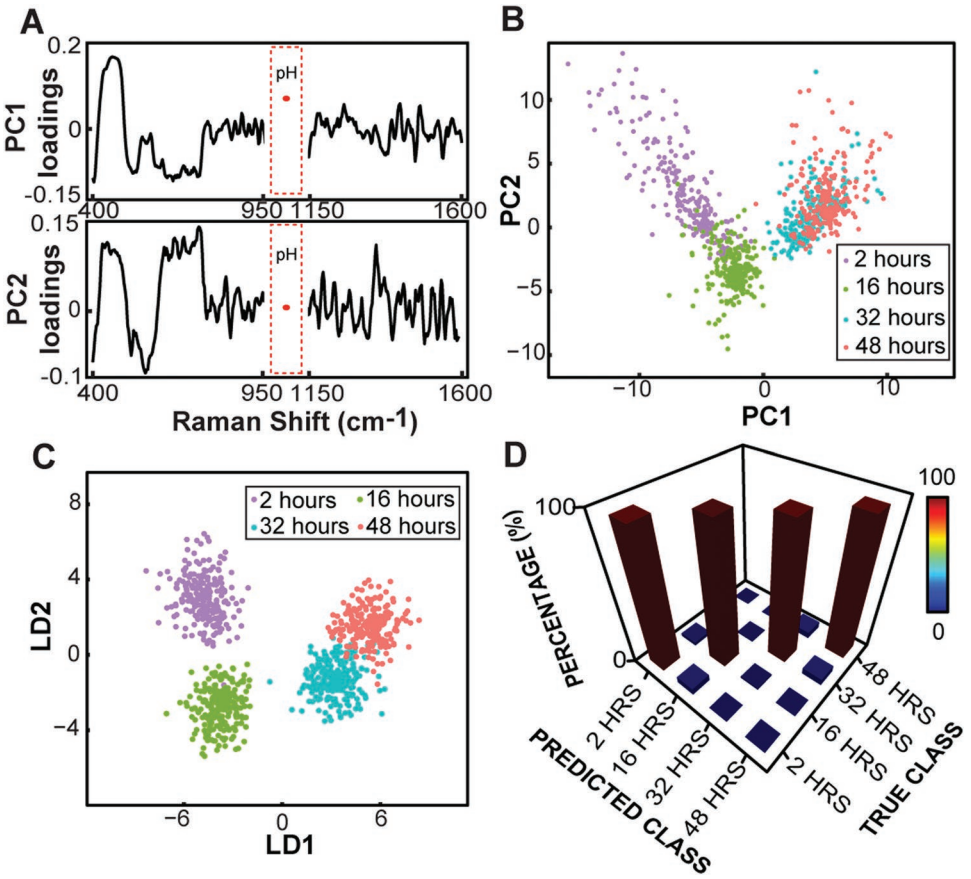

Figure 5. Multivariate classification of SERS datasets between different biofilm growth times. A) PC1 and PC2 loading spectra, B) PC score scatter plots, and C) PCA-LDA score scatter plots for the measured SERS spectra from different *E. coli* biofilm growth times. D) Histograms of a confusion matrix for PCA-LDA with LOOCV.

the PCA-LDA model can achieve an overall accuracy of 96.57%. (Figure 5D; Table S2, Supporting Information).

7. Conclusion

In conclusion, we have created transparent nanoplasmonic microporous meshes, consisting of uniformly-structured nanolaminated plasmonic nanoantennas on microporous polymeric meshes, for spatiotemporal multimodal SERS measurements at the bio-interface. We report a high-throughput fabrication process using reverse nanoimprint lithography, which features several enabling novelties: 1) the RNIL process can enable high-throughput generation of polymeric NHA physical deposition masks, facile transfer of the NHA array masks onto substrates, and continuous contact between the mask and micro/nanostructured substrates for generating uniformly shaped multilayered nanodisks via a line-of-sight deposition process, and 2) the RIE process can allow tailoring of the base diameter of the multilayered nanodisks for engineering the plasmonic modes. This CMOS-compatible fabrication process can potentially enable the high-throughput transfer of plasmonic nanoantennas onto micro/nanostructured electrical or optical devices, opening exciting avenues for integrated electro-optic devices that can allow multifunctional operation at the nanoscale such as integrated electrical and optical sensors for high-order chemical sensing at the bio-interface in complex biosystems.[51] We demonstrate that the BTNMMs, due to their unique structural characteristics (e.g., ultrathin and porous geometry) and optical properties (e.g., optical transparency and uniformly distributed engineered plasmonic hotspots), allow spatiotemporal SERS measurements in both targeted and non-targeted modalities simultaneously by stacking labeled and label-free devices. To illustrate the feasibility of multimodal spatiotemporal SERS, we demonstrate that the BTNMMs can resolve the diffusion dynamics of hydroxyl ions, adenine molecules, and R6G molecules in agarose gel; in qualitative agreement with a theoretically developed model describing their diffusion dynamics. Furthermore, the BTNMMs can seamlessly interface multicellular networks due to their biomechanical compatibility and transport permeability. As a proof-of-concept demonstration, we illustrate that the BTNMMs can act as bio-interfaced multifunctional sensors for the in situ spatiotemporal SERS monitoring of *E. coli* biofilms in targeted pH sensing and non-targeted molecular profiling. Since the bacterial biofilm development processes are spatiotemporally coupled with changes in local pH and biomolecule concentrations, resolving the spatiotemporal evolution of pH and different biochemical components can potentially assist therapeutic intervention. Looking forward, we envision that the BTNMMs, demonstrating both ultrasensitive multimodal

sensing capability and a seamless interface with multicellular biological systems, can pave the way for exciting bio-interfaced multifunctional sensing applications both in vitro (e.g., biosensing scaffolds for drug discovery studies in bacterial biofilms and 3D cell culture models) and in vivo (e.g., implantable probes for long term disease diagnostics).

8. Experimental Section

Fabrication of PFPE Nano-Templates: A silicon template consisting of a 2D square nanowell array (diameter: 120 nm, height: 300 nm, periodicity: 400 nm) was used as a master mold for replicating the PFPE nano-templates (Fluorolink PFPE, Solvay, Belgium) using UV nanoimprint lithography. The UV nanoimprint lithography process consisted of UV curing under 2 bar pressure for 3 min, a second round of UV curing under vacuum for 3 min, and post-annealing for 45 min at 100 °C.

Fabrication of Micro-Templates for Creating TMNNs: Omnicoat (Kayaku Advanced Materials Inc., USA) was spin-coated on Si wafers at 3000 rpm for 30 s, followed by baking at 200 °C for 1 min. Subsequently, a negative-tone photoresist (SU8-2002, Kayaku Advanced Materials Inc.) was used to generate microwell arrays (diameter: 16 µm, height: 2 µm, periodicity: 64 µm) on the Omnicoat coated silicon wafers using conventional photolithography.

Fabrication of SU8 Micropillars: Micropillar arrays (diameter: 8 µm, height: 2 µm, periodicity: 16 µm) made of SU8-2002 were created on silicon wafers using conventional photolithography.

Fabrication of PMMA Nanohole Array Masks: First, a 16% (w/w) solution of PMMA (molecular weight = 15k) was spin-coated in anisole on the PFPE nano-template at 5000 rpm for 30 s. Then, the solvent was evaporated by baking the template at 180 °C for 2 min to create PMMA NHAs within the PFPE nano-template. Then, the PMMA NHAs were transferred onto the target substrates using thermal reverse nanoimprint lithography. The following conditions were used for thermal reverse nanoimprint lithography: time = 10 min, pressure = 2 bar, and temperature = 170 °C. Finally, RIE (RIE-1C, Samco, Japan) was performed in the plasma of O_2 (30 sccm) under the RF power of 30 W for removing the residual PMMA and tuning the nanohole size.

Fabrication of NLPNAs: E-beam evaporation (PVD250, Kurt J. Lesker, USA) was used to deposit alternating layers of Au (25 nm) and SiO_2 (8 and 12 nm from bottom) on the substrates through the PMMA nanohole array mask. Additionally, 0.7 nm of titanium was deposited between the Au and SiO_2 layers, and 1 nm of chrome between the Au layer and the substrate for adhesion. Then, the PMMA was dissolved in anisole at 70 °C to generate the NLPNAs. Subsequently, RIE (RF power = 30 W) was performed in the plasma of O_2 (30 sccm) to remove any residual anisole. Lastly, BOE 10:1 was used to open the dielectric nanogaps. (Transene Inc., USA).

Release of BTNMMs from the Silicon Substrate: Omnicoat was developed using Microposit MF-319 (Kayaku Advanced Materials Inc.) to release the BTNMMs from the silicon substrate. Using a Pasteur pipette, the BTNMMs were placed in DI water and rinsed 3 times.

Transmittance Measurements: A UV–vis–NIR spectrophotometer (Cary 5000, Agilent, USA) was used to measure the transmittance spectra.

FDTD Simulation: A uniform 3 nm mesh was used in *x*-, *y*-, and *z*-directions. The optical constants of Au were taken from Johnson and Christy. The Bloch boundary condition was used in *x*- and *y*-directions with a periodicity of 400 nm, and the perfectly matched layer boundary condition was used in the *z*-direction. The refractive indices of SiO_2 and SU8 were set as 1.50 and 1.57, respectively.

BZT SERS Measurements: A 10^{-3} M BZT solution in ethanol was prepared. A self-assembled monolayer of BZT was generated on the NLPNAs by incubating the samples in the BZT solution for 24 h. For the SERS experiments, a confocal Raman microscope (alpha 300 RSA+, WItec, Germany) was used under 785 nm laser excitation (Xtra II, Toptica, Germany) via a 20× objective lens. To detect the backscattered photons, a spectrometer (UHTS300, WItec, Germany) containing a CCD camera (DU401A, Oxford Instruments, UK) was used. The laser power and acquisition time for the BZT SERS measurements were 0.4 mW and 0.1 s respectively. Baseline correction and cosmic ray removal were performed after acquiring the signals using the Project v4.1 Software (WITec, Germany).

Calculation of SERS EF: For calculating The SERS EF, the following equation was used: $EF = (I_{SERS}/I_{Raman}) \times (N_{Raman}/N_{SERS})$, where I_{SERS} is the measured BZT SERS intensity, I_{Raman} is the Raman intensity of BZT, and $N_{SERS,}$ and N_{Raman} are the number of BZT molecules contributing to SERS and Raman intensities respectively. For calculating I_{Raman} and I_{SERS}, the 1094 and 1070 cm^{-1} Raman peak intensities were used, which originate from the C–C–C ring in-plane breathing mode with C–S stretching mode. To calculate $N_{SERS,}$ the following equation was used: $N_{SERS} = SA \times \rho_{SERS}$, where SA is the surface area of the SERS substrates under the focused illumination contributing to the enhancement of Raman signals and ρ_{SERS} is the packing density of BZT on Au surface (6.8×10^{14} molecules cm^{-2}). To calculate N_{Raman}, the equation was used: $N_{Raman} = A \times d_{eff} \times \rho_{BZT}$, where A is the area of the focused illumination, d_{eff} is the effective focus depth of laser beam spot in the BZT solution, and ρ_{BZT} is the density of BZT molecules in the solution (5.9×10^{21} molecules cm^{-3}). The d_{eff} was calculated by measuring the intensity of the silicon Raman peak (527 cm^{-1}) at varying distances between a silicon wafer and the objective lens.

SERS Enabled pH Detection: The samples were incubated in a 10 µM ethanolic 4-MPy solution for 1 h to generate a self-assembled monolayer. After 4-MPy functionalization, the samples were immersed in 1k-PEG-thiol (0.5% weight ratio) for 1 h for stabilization. For generating the pH calibration curve, the sample was immersed in 1× PBS solution with varying pH values (pH = 4 to 10), and the SERS spectrum was collected.

Multimodal SERS Detection of Alkaline Solution with R6G and Adenine: Two percent agar powder was dissolved in 1× PBS (pH = 7), the solution was boiled in a microwave, and placed in water bath at 50 °C. A portion of the agarose solution was poured into a petri dish and cooled down until solidification. Then, the 4-MPy functionalized BTNMM was captured on a PET sheet and gently transferred onto the agarose gel. Subsequently, the label-free BTNMM was transferred onto the agarose gel on top of the 4-MPy functionalized BTNMM. Then, the remaining agarose gel was poured into the petri dish to embed the BTNMMs within the gel matrix. A solution containing 10^{-3} M adenine (molecular weight = 135.13 g mol^{-1}, Sigma–Aldrich) and 10^{-3} M Rhodamine 6G (molecular weight = 479.02 g mol^{-1}, Sigma–Aldrich) in 1× PBS (pH = 10) was prepared. A small reservoir was created in the agarose gel using a scalpel and 10 µl of the solution was added to the reservoir. The reservoir was refilled with the solution every 6 h and SERS measurements were performed via a 20× objective lens with 2 mW power and 1 s integration time over a 16 mm^2 region containing 400 pixels.

Bacterial Cell Culture: Stock solution of bacterial strain *E. coli* ATCC 25922 was streaked on LB agar plates and grown at 37 °C for 24 h. An inoculating loop was used to transfer a single colony to a tube containing 15 mL of LB broth and the tube was placed in 37 °C with agitation at 200 rpm for 24 h. Hundred microliters of the obtained bacterial culture were washed with 10 ml of LB broth (3 times) by centrifugation (4,000 rpm and 8 min) and re-suspended in 10 ml of fresh broth. For quantifying the concentration of *E. coli*, serial dilution of the bacterial suspensions was performed in LB broth, serially diluted bacterial suspensions were grown on LB agar plates at 37 °C, and the colony-forming units (CFUs) were counted after 24 h.

Bio-Interfaced SERS Monitoring of E. coli Biofilm Development: The 4-MPy functionalized BTNMM was captured on a PET sheet and gently transferred onto an LB agar plate. Subsequently, the label-free BTNMM was transferred onto the LB agar plate on top of the 4-MPy functionalized BTNMM. The system by sterilized with UV light for 1 h. Then, 10 µl of the bacterial suspension in fresh LB broth was drop-casted on the stacked BTNMMs. SERS measurements were performed via a 20× objective lens with 1 mW power and 2 s integration time over a 16 mm^2 region containing 400 pixels at various times. Between SERS measurements, the plate was stored at 37 °C. To determine viable bacteria, the top portion was scrapped off of the LB agar containing bacteria along

with the BTNMMs using an inoculating loop and transferred to a vial containing 1 ml PBS, followed by sonication. For quantifying the concentration of *E. coli*, serial dilution of the bacterial suspensions was performed in LB broth, serially diluted bacterial suspensions were grown on LB agar plates at 37 °C, and the CFUs were counted after 24 h.

Biofilm Staining and Fluorescence Imaging: Fifty microliters of Calcofluor White stain (Sigma–Aldrich) was added to 1 ml of DI water. Then, the diluted stain was drop-casted on the LB agar plates containing the stacked BTNMMs with *E. coli* biofilms. The plates were stored in the dark for 20 min and subsequently rinsed with 1× PBS to minimize the background fluorescence. Fluorescence imaging was performed using an LED light cube (excitation: 360 nm, emission: 447 nm) on the EVOS-FL auto system (Thermo Fischer Scientific, USA).

Data Analysis: Baseline correction, cosmic ray removal, and spectral filtering via Savitzy Golay filtering were performed using the Project v4.1 Software. The SERS data was normalized using the plasmonic electronic Raman scattering (ERS) signals, reflected by the pseudo peak at 77 cm^{-1}, as the internal standards. This normalization method had previously been applied for various biological applications.[19,28,52] Data truncation was performed using MATLAB. Lastly, R software was used for performing PCA and LDA.

Supporting Information

Supporting Information is available from the Wiley Online Library or from the author.

Acknowledgements

This work was supported by AFOSR Young Investigator Award FA9550-18-1-0328 and by the US National Science Foundation grants OISE-1545756, CBET-2029911, CBET-2231807, and DMR-2139317. Laboratory and instrumentation support was provided by NanoEarth—a node of the NSF-supported NNCI (NSF award number #1542100). Additional support was provided by the Sustainable Nanotechnology Interdisciplinary Graduate Program (VTSuN IGEP), funded by Virginia Tech.

Conflict of Interest

The authors declare no conflict of interest.

Data Availability Statement

The data that support the findings of this study are available from the corresponding author upon reasonable request.

Keywords

bacterial biofilms, bio-interfaced surface-enhanced Raman spectroscopy (SERS), mesh devices, multimodal surface-enhanced Raman spectroscopy (SERS), nanoimprint lithography, surface-enhanced Raman spectroscopy (SERS)

Received: July 21, 2022
Published online: September 26, 2022

[1] W. Du, O. Elemento, *Oncogene* **2015**, *34*, 3215.
[2] K. Bisht, C. A. Wakeman, *Front. Microbiol.* **2019**, *10*, 1908.
[3] a) P. S. Stewart, *Int. J. Med. Microbiol.* **2002**, *292*, 107; b) D. Sharma, L. Misba, A. U. Khan, *Antimicrob. Resist. Infec. Control* **2019**, *8*, 76.
[4] N. B. S. Silva, L. Marques, D. Röder, *J. Appl. Microbiol.* **2021**, *131*, 2148.
[5] C. A. Fux, J. W. Costerton, P. S. Stewart, P. Stoodley, *Trends Microbiol.* **2005**, *13*, 34.
[6] a) M. Prax, R. Bertram, *Front. Cell. Infect. Microbiol.* **2014**, *4*, 148; b) S. M. Amato, M. P. Brynildsen, *PLoS One* **2014**, *9*, e93110.
[7] a) A. P. Roberts, P. Mullany, *Expert Rev. Anti-Infect. Ther.* **2010**, *8*, 1441; b) T.-F. Mah, *Future Microbiol.* **2012**, *7*, 1061.
[8] a) S. Kjelleberg, S. Molin, *Curr. Opin. Microbiol.* **2002**, *5*, 254; b) P. Saxena, Y. Joshi, K. Rawat, R. Bisht, *Indian J. Microbiol.* **2019**, *59*, 3.
[9] G. Orazi, G. A. O'Toole, *J. Bacteriol.* **2019**, *202*, e00530.
[10] a) F. R. Cockerill, III, *Archi. Pathol. Lab. Med.* **2003**, *127*, 1112; b) E. Engvall, *Med. Biol.* **1977**, *55*, 193.
[11] a) N. AlMasoud, H. Muhamadali, M. Chisanga, H. AlRabiah, C. A. Lima, R. Goodacre, *Analyst* **2021**, *146*, 770; b) W. B. Dunn, D. I. Broadhurst, H. J. Atherton, R. Goodacre, J. L. Griffin, *Chem. Soc. Rev.* **2011**, *40*, 387.
[12] a) J. Azeredo, N. F. Azevedo, R. Briandet, N. Cerca, T. Coenye, A. R. Costa, M. Desvaux, G. Di Bonaventura, M. Hébraud, Z. Jaglic, *Crit. Rev. Microbiol.* **2017**, *43*, 313; b) I. Dige, H. Nilsson, M. Kilian, B. Nyvad, *Eur. J. Oral Sci.* **2007**, *115*, 459; c) W. Manz, K. Wendt-Potthoff, T. Neu, U. Szewzyk, J. Lawrence, *Microb. Ecol.* **1999**, *37*, 225.
[13] a) T.-H. Kim, D. Lee, J.-W. Choi, *Biosens. Bioelectron.* **2017**, *94*, 485; b) T. Haruyama, *Adv. Drug Delivery Rev.* **2003**, *55*, 393.
[14] a) C. Zong, M. Xu, L.-J. Xu, T. Wei, X. Ma, X.-S. Zheng, R. Hu, B. Ren, *Chem. Rev.* **2018**, *118*, 4946; b) J. Langer, D. Jimenez de Aberasturi, J. Aizpurua, R. A. Alvarez-Puebla, B. Auguié, J. J. Baumberg, G. C. Bazan, S. E. Bell, A. Boisen, A. G. Brolo, *ACS Nano* **2019**, *14*, 28.
[15] a) Y. C. Cao, R. Jin, J.-M. Nam, C. S. Thaxton, C. A. Mirkin, *J. Am. Chem. Soc.* **2003**, *125*, 14676; b) Y. C. Cao, R. Jin, C. A. Mirkin, *Science* **2002**, *297*, 1536.
[16] a) S. W. Bishnoi, C. J. Rozell, C. S. Levin, M. K. Gheith, B. R. Johnson, D. H. Johnson, N. J. Halas, *Nano Lett.* **2006**, *6*, 1687; b) S. Hu, B.-J. Liu, J.-M. Feng, C. Zong, K.-Q. Lin, X. Wang, D.-Y. Wu, B. Ren, *J. Am. Chem. Soc.* **2018**, *140*, 13680.
[17] a) D. W. Li, L. L. Qu, K. Hu, Y. T. Long, H. Tian, *Angew. Chem.* **2015**, *127*, 12949; b) D. Yang, S. Afroosheh, J. O. Lee, H. Cho, S. Kumar, R. H. Siddique, V. Narasimhan, Y.-Z. Yoon, A. T. Zayak, H. Choo, *Anal. Chem.* **2018**, *90*, 14269.
[18] a) X.-S. Zheng, P. Hu, Y. Cui, C. Zong, J.-M. Feng, X. Wang, B. Ren, *Anal. Chem.* **2014**, *86*, 12250; b) Y. Shen, L. Liang, S. Zhang, D. Huang, J. Zhang, S. Xu, C. Liang, W. Xu, *Nanoscale* **2018**, *10*, 1622; c) S. Kang, W. Nam, W. Zhou, I. Kim, P. J. Vikesland, *ACS Appl. Nano Mater.* **2021**, *4*, 5768.
[19] W. Nam, X. Ren, I. Kim, J. Strobl, M. Agah, W. Zhou, *Anal. Chem.* **2021**, *93*, 4601.
[20] a) M. Erzina, A. Trelin, O. Guselnikova, B. Dvorankova, K. Strnadova, A. Perminova, P. Ulbrich, D. Mares, V. Jerabek, R. Elashnikov, *Sens. Actuators, B* **2020**, *308*, 127660; b) Y.-C. Kao, X. Han, Y. H. Lee, H. K. Lee, G. C. Phan-Quang, C. L. Lay, H. Y. F. Sim, V. J. X. Phua, L. S. Ng, C. W. Ku, *ACS Nano* **2020**, *14*, 2542; c) H. Shin, S. Oh, S. Hong, M. Kang, D. Kang, Y.-g. Ji, B. H. Choi, K.-W. Kang, H. Jeong, Y. Park, *ACS Nano* **2020**, *14*, 5435; d) W. J. Thrift, S. Ronaghi, M. Samad, H. Wei, D. G. Nguyen, A. S. Cabuslay, C. E. Groome, P. J. Santiago, P. Baldi, A. I. Hochbaum, *ACS Nano* **2020**, *14*, 15336.
[21] a) Y. Ren, C. Wang, Z. Chen, E. Allan, H. C. van der Mei, H. J. Busscher, *FEMS Microbiol. Rev.* **2018**, *42*, 259; b) P. S. Stewart, M. J. Franklin, *Nat. Rev. Microbiol.* **2008**, *6*, 199.
[22] S. Fulaz, D. Hiebner, C. H. N. Barros, H. Devlin, S. Vitale, L. Quinn, E. Casey, *ACS Appl. Mater. Interfaces* **2019**, *11*, 32679.

[23] P. Stoodley, K. Sauer, D. G. Davies, J. W. Costerton, *Annu. Rev. Microbiol.* **2002**, *56*, 187.
[24] X. Wang, S.-C. Huang, S. Hu, S. Yan, B. Ren, *Nat. Rev. Phys.* **2020**, *2*, 253.
[25] a) X. Sun, H. Li, *Curr. Nanosci.* **2016**, *12*, 175; b) S.-C. Luo, K. Sivashanmugan, J.-D. Liao, C.-K. Yao, H.-C. Peng, *Biosens. Bioelectron.* **2014**, *61*, 232.
[26] Y. Chen, *Microelectron. Eng.* **2015**, *135*, 57.
[27] A. Leitis, M. L. Tseng, A. John-Herpin, Y. S. Kivshar, H. Altug, *Adv. Mater.* **2021**, *33*, 2102232.
[28] A. Garg, E. Mejia, W. Nam, M. Nie, W. Wang, P. Vikesland, W. Zhou, *Small* **2022**, *18*, 2106887.
[29] J. Song, W. Zhou, *Nano Lett.* **2018**, *18*, 4409.
[30] C. C. Liang, C. H. Lin, T. C. Cheng, J. Shieh, H. H. Lin, *Adv. Mater. Interfaces* **2015**, *2*, 1500030.
[31] W. Nam, J. Song, S. A. Safiabadi Tali, H. J. Lezec, A. Agrawal, W. Zhou, *ACS Appl. Nano Mater.* **2021**, *4*, 3175.
[32] J. Song, W. Nam, W. Zhou, *Adv. Mater. Technol.* **2019**, *4*, 1800689.
[33] a) J. Henzie, M. H. Lee, T. W. Odom, *Nat. Nanotechnol.* **2007**, *2*, 549; b) W. Zhou, M. Dridi, J. Y. Suh, C. H. Kim, D. T. Co, M. R. Wasielewski, G. C. Schatz, T. W. Odom, *Nat. Nanotechnol.* **2013**, *8*, 506; c) A. Fernandez-Bravo, D. Wang, E. S. Barnard, A. Teitelboim, C. Tajon, J. Guan, G. C. Schatz, B. E. Cohen, E. M. Chan, P. J. Schuck, *Nat. Mater.* **2019**, *18*, 1172.
[34] a) N. Farmakidis, N. Youngblood, X. Li, J. Tan, J. L. Swett, Z. Cheng, C. D. Wright, W. H. P. Pernice, H. Bhaskaran, *Sci. Adv.* **2019**, *5*, eaaw2687; b) A. Tuniz, O. Bickerton, F. J. Diaz, T. Käsebier, E.-B. Kley, S. Kroker, S. Palomba, C. M. de Sterke, *Nat. Commun.* **2020**, *11*, 2413; c) T. J. Davis, D. E. Gómez, A. Roberts, *Nanophotonics* **2017**, *6*, 543.
[35] I. Zoric, M. Zach, B. Kasemo, C. Langhammer, *ACS Nano* **2011**, *5*, 2535.
[36] a) M. Frederiksen, V. E. Bochenkov, R. Ogaki, D. S. Sutherland, *Nano Lett.* **2013**, *13*, 6033; b) G. Schaffernak, M. K. Krug, M. Belitsch, M. Gašparić, H. Ditlbacher, U. Hohenester, J. R. Krenn, A. Hohenau, *ACS Photonics* **2018**, *5*, 4823; c) E. Mejia, Y. Qian, S. Safiabadi Tali, J. Song, W. Zhou, *Appl. Phys. Lett.* **2021**, *118*, 241108.
[37] L. Bi, Y. Wang, Y. Yang, Y. Li, S. Mo, Q. Zheng, L. Chen, *ACS Appl. Mater. Interfaces* **2018**, *10*, 15381.
[38] S. Kang, W. Nam, W. Zhou, I. Kim, P. J. Vikesland, *ACS Appl. Nano Mater.* **2021**, *4*, 5768.
[39] W. Nam, Y. Zhao, J. Song, S. A. Safiabadi Tali, S. Kang, W. Zhu, H. J. Lezec, A. Agrawal, P. J. Vikesland, W. Zhou, *J. Phys. Chem. Lett.* **2020**, *11*, 9543.
[40] A. Garg, W. Nam, W. Zhou, *ACS Appl. Mater. Interfaces* **2020**, *12*, 56290.
[41] K. Samprovalaki, P. Robbins, P. Fryer, *J. Food Eng.* **2012**, *111*, 537.
[42] a) N. Fatin-Rouge, K. Starchev, J. Buffle, *Biophys. J.* **2004**, *86*, 2710; b) M. A. Lauffer, *Biophys. J.* **1961**, *1*, 205.
[43] W. R. Premasiri, J. C. Lee, A. Sauer-Budge, R. Théberge, C. E. Costello, L. D. Ziegler, *Anal. Bioanal. Chem.* **2016**, *408*, 4631.
[44] a) C. Wei, M. Li, X. Zhao, *Front. Microbiol.* **2018**, *9*, 2857; b) H. Nikaido, T. Nakae, *Adv. Microb. Physiol.* **1980**, *20*, 163.
[45] a) S. De Marchi, G. Bodelon, L. Vazquez-Iglesias, L. M. Liz-Marzan, J. Perez-Juste, I. Pastoriza-Santos, *Appl. Mater. Today* **2019**, *14*, 207; b) D. Wang, X. Ding, P. N. Rather, *J. Bacteriol.* **2001**, *183*, 4210.
[46] a) Y. Chao, T. Zhang, *Anal. Bioanal. Chem.* **2012**, *404*, 1465; b) S. Keleştemur, M. Çulha, *Appl. Spectrosc.* **2017**, *71*, 1180; c) N. N. Wickramasinghe, M. M. Hlaing, J. T. Ravensdale, R. Coorey, P. S. Chandry, G. A. Dykes, *Sci. Rep.* **2020**, *10*, 16457; d) H.-C. Flemming, T. R. Neu, D. J. Wozniak, *J. Bacteriol.* **2007**, *189*, 7945.
[47] a) P. Merkl, M.-S. Aschtgen, B. Henriques-Normark, G. A. Sotiriou, *Biosens. Bioelectron.* **2021**, *171*, 112732; b) B. Hollmann, M. Perkins, V. M. Chauhan, J. W. Aylott, K. R. Hardie, *npj Biofilms Microbiomes* **2021**, *7*, 50.
[48] a) J. W. Costerton, *J. Ind. Microbiol. Biotechnol.* **1995**, *15*, 137; b) R. M. Donlan, *Emerging Infect. Dis.* **2002**, *8*, 881.
[49] a) K. Ranjith, J. Ramchiary, J. S. Prakash, K. Arunasri, S. Sharma, S. Shivaji, *Front. Microbiol.* **2019**, *10*, 1308; b) S. R. Martinez, L. E. Ibarra, R. A. Ponzio, M. V. Forcone, A. B. Wendel, C. A. Chesta, M. B. Spesia, R. E. Palacios, *ACS Infect. Dis.* **2020**, *6*, 2202; c) S. E. Cowan, E. Gilbert, D. Liepmann, J. D. Keasling, *Appl. Environ. Microbiol.* **2000**, *66*, 4481.
[50] C. Fei, S. Mao, J. Yan, R. Alert, H. A. Stone, B. L. Bassler, N. S. Wingreen, A. Košmrlj, *Proc. Natl. Acad. Sci. USA* **2020**, *117*, 7622.
[51] A. Hierlemann, R. Gutierrez-Osuna, *Chem. Rev.* **2008**, *108*, 563.
[52] W. Wang, S. Kang, P. J. Vikesland, *Environ. Sci. Technol.* **2021**, *55*, 9119.